

Cryo-EM structures of human magnesium channel MRS2 reveal gating and regulatory mechanisms

Received: 22 August 2023

Accepted: 16 October 2023

Published online: 08 November 2023

 Check for updatesLouis Tung Faat Lai¹, Jayashree Balaraman¹, Fei Zhou¹ & Doreen Matthies¹ ✉

Magnesium ions (Mg^{2+}) play an essential role in cellular physiology. In mitochondria, protein and ATP synthesis and various metabolic pathways are directly regulated by Mg^{2+} . MRS2, a magnesium channel located in the inner mitochondrial membrane, mediates the influx of Mg^{2+} into the mitochondrial matrix and regulates Mg^{2+} homeostasis. Knockdown of MRS2 in human cells leads to reduced uptake of Mg^{2+} into mitochondria and disruption of the mitochondrial metabolism. Despite the importance of MRS2, the Mg^{2+} translocation and regulation mechanisms of MRS2 are still unclear. Here, using cryo-EM we report the structures of human MRS2 in the presence and absence of Mg^{2+} at 2.8 Å and 3.3 Å, respectively. From the homo-pentameric structures, we identify R332 and M336 as major gating residues, which are then tested using mutagenesis and two cellular divalent ion uptake assays. A network of hydrogen bonds is found connecting the gating residue R332 to the soluble domain, potentially regulating the gate. Two Mg^{2+} -binding sites are identified in the MRS2 soluble domain, distinct from the two sites previously reported in CorA, a homolog of MRS2 in prokaryotes. Altogether, this study provides the molecular basis for understanding the Mg^{2+} translocation and regulatory mechanisms of MRS2.

Magnesium (Mg^{2+}), the most abundant divalent cation in living organisms, plays an essential role in many biological processes, including ATP synthesis and hydrolysis, DNA replication, protein synthesis, modulation of enzymatic activity, and protein stability^{1,2}. It acts as a cofactor of more than 600 enzymes, including protein kinases, ATPases, exonucleases, and other nucleotide-related enzymes. It has been shown that Mg^{2+} is involved in various physiological functions such as muscle contraction, vasodilation, neuronal signaling, and immunity¹⁻³. Intracellular Mg^{2+} concentrations are tightly regulated and dysregulation of Mg^{2+} homeostasis is associated with diseases including muscular dysfunction, bone wasting, immunodeficiency, cardiac syndromes, neuronal disorders, obesity, Parkinson's disease, and cancer^{2,4-6}.

The total Mg^{2+} content in cells amounts to between 17–30 mM, however, most Mg^{2+} is bound to ATP and other molecules, resulting in

much lower free Mg^{2+} concentrations between 0.5–1.2 mM^{2,7}. In mitochondria, where ATP synthesis and various metabolic processes occur, Mg^{2+} modulates enzymes involved in tricarboxylic acid cycle (TCA), oxidative metabolism and directly participates in mitochondrial metabolism in form of $MgATP^{2,8,9}$. Although the high inner mitochondrial membrane potential (about –180 mV) can theoretically drive a large electrophoretic Mg^{2+} influx into the mitochondrial matrix, the free Mg^{2+} concentration in the matrix is found to be comparable to that in the cytosol (–0.8 mM), implying Mg^{2+} transport is tightly regulated in order to maintain normal mitochondrial physiology¹⁰. Most of the Mg^{2+} influx into mitochondria is mediated by the Mitochondrial RNA Splicing 2 (MRS2) channel, located in the inner mitochondrial membrane¹¹⁻¹⁴. Knockdown of MRS2 in human cells leads to reduced uptake of Mg^{2+} into mitochondria, loss of respiratory complex I, disruption of mitochondrial metabolism, and cell death^{15,16}. A loss of

¹Unit on Structural Biology, Division of Basic and Translational Biophysics, Eunice Kennedy Shriver National Institute of Child Health and Human Development, National Institutes of Health, Bethesda, MD 20892, USA. ✉e-mail: doreen.matthies@nih.gov

function mutation disrupting MRS2 is also associated with demyelination syndrome in rats¹⁷. Recent studies in mice show that MRS2 is required for lactate-mediated Mg^{2+} -uptake in mitochondria¹⁸, and knockout of MRS2 causes reprogramming of the metabolism including upregulation of thermogenesis, oxidative phosphorylation and fatty acid catabolism via HIF1 α transcriptional regulation¹⁹. Despite the physiological implications of MRS2, little is known about its Mg^{2+} translocation and regulatory mechanisms.

MRS2 belongs to the CorA protein superfamily characterized by a highly conserved Glycine-Methionine-Asparagine (GMN) motif in the loop between transmembrane helix 1 and 2. In prokaryotes, CorA regulates the intracellular Mg^{2+} concentration through a negative feedback mechanism, where at low Mg^{2+} concentrations, unbinding of Mg^{2+} ions from the CorA soluble domain favors a series of conductive states, allowing Mg^{2+} permeation^{20,21}. MRS2 and CorA only share a sequence identity of ~14%, so insight into MRS2 Mg^{2+} translocation and regulatory mechanism based on CorA has been limited. Until very recently, the only MRS2 structure reported is the monomeric N-terminal soluble domain of yeast MRS2²², lacking the transmembrane domain. A recent study of the N-terminal domain of human MRS2 revealed it forms a dimer, contrasting the pentameric assembly of CorA²³. However, the missing structural information of the MRS2 full-length protein including the pore region hampers the understanding of how Mg^{2+} translocation occurs through the pore and how MRS2 is regulated.

Here, we use single particle cryo-EM to determine the structures of human MRS2 in the presence and absence of Mg^{2+} . N-terminal sequencing of MRS2 revealed the mitochondrial transit peptide cleavage site at residue 71. From the homo-pentameric structures, M336 and R332 are identified as key gating residues, which are further tested by mutagenesis, and Mg^{2+} -dependent growth and Ni^{2+} -sensitivity assays. The structures also reveal that MRS2 possesses two Mg^{2+} -binding motifs in the soluble domain between neighboring subunits, which are different from known bacterial CorA structures. Finally, an inter-subunit salt bridge between R116 and E291 in the soluble domain is found. Disruption of this salt bridge leads to an increase in channel activity. Altogether, this study provides insight into how translocation of Mg^{2+} is mediated via MRS2 and how it is regulated.

Results

Expression, purification, and biochemical characterization of human MRS2

MRS2, a mitochondrial membrane protein encoded in chromosome 6 of the nuclear genome, possesses a mitochondrial transit peptide (MTP) at its N-terminus, which is cleaved after translocation into the inner mitochondrial membrane. As such, we expressed human MRS2 conjugated with a C-terminal FLAG tag in Expi293F cells and purified it in the presence of Mg^{2+} using affinity and size-exclusion chromatography (Supplementary Fig. 1). Purified MRS2 shows a band slightly above 38 kDa based on SDS-PAGE (Supplementary Fig. 1b), which is smaller than the full-length size at 51 kDa, suggesting the N-terminal MTP has been cleaved in purified MRS2. Native-PAGE of purified MRS2 shows a major band between the native marker at 242 kDa and 480 kDa indicating MRS2 assembles into an oligomer (Supplementary Fig. 1c). Negative-staining EM followed by 2D classification of MRS2 particles shows a funnel-shaped structure, resembling that observed in CorA (Supplementary Fig. 1d). To identify the cleavage site of the MTP in human MRS2, online prediction web servers were initially used. The cleavage site was not detected using Target-2.0²⁴ and SignalP-6.0²⁵, while it was predicted at residue 21 by Mitofates²⁶. These prediction results were contrary to the Uniport entry (Q9HD23) which suggested a cleavage at residue 50. Here, we used an experimental approach, N-terminal sequencing, of purified human MRS2 and the first amino acid detected is residue 71 starting with threonine (Supplementary Fig. 1e). To confirm the identity of the MTP, full-length MRS2 or

truncated MRS2(71-443) conjugated with GFP were expressed in Expi293F cells and imaged using confocal microscopy. It shows that the full-length MRS2-GFP localizes in mitochondria (Supplementary Fig. 1f), while MRS2(71-443)-GFP can no longer be imported into mitochondria and largely localizes in the ER (Supplementary Fig. 1g).

Structural analysis of human MRS2 in the presence of Mg^{2+} using cryo-EM

Cryo-EM images of purified MRS2 were recorded using a 300 kV Titan Krios equipped with a K3 camera and energy filter (Supplementary Fig. 2a). Initial 2D class averages (Supplementary Fig. 2b) confirmed the by negative-staining EM observed pentameric arrangement of human MRS2, which has been shown for bacterial^{21,27–31} and archaeal³² members of this protein family and is contrary to the most recent prediction of human MRS2 to form a dimer²³. The final 3D reconstruction of MRS2 in the presence of Mg^{2+} (referred to as MRS2- Mg^{2+}) with C5 symmetry and without symmetry applied (C1) resulted in maps with average resolutions of 2.8 Å and 3.1 Å, respectively, with the highest local resolution estimated to be 2.3 Å (Fig. 1 and Supplementary Figs. 2c–f, 3–4).

The human MRS2 pentamer exhibits a funnel-shaped structure with dimensions of approximately 130 Å by 100 Å by 100 Å (H x W x D) (Fig. 1). No ordered density representing detergent molecule or co-purified lipid is observed in the transmembrane region. The overall architecture of MRS2 resembles that of homologs in the CorA superfamily including *TmCorA*^{21,27–30}, *EcCorA*³¹, *MjCorA*³², *EcZntB*³³, and *PaZntB*³⁴ (Supplementary Fig. 5), even though they share low sequence identity (Supplementary Fig. 6).

Each of the human MRS2 protomers consists of a large N-terminal soluble domain facing the mitochondrial matrix side. The N-terminal soluble domain is composed of six anti-parallel β -strands and seven α -helices arranged in a $\alpha/\beta/\alpha$ fold manner (Fig. 1c, d). The arrangement of the $\alpha/\beta/\alpha$ fold in MRS2 is different from that of *TmCorA*, which possess seven anti-parallel β -strands and six α -helices (Fig. 1d and Supplementary Fig. 5). The soluble domain connects to the long $\alpha 8$ /TM1 helix spanning a total of 71 residues (residues 290–360). The $\alpha 8$ /TM1 helix starts from the far matrix side of MRS2 while the C-terminal part of $\alpha 8$ enters the inner mitochondrial membrane, serving as the first transmembrane helix TM1. Following the long $\alpha 8$ /TM1 helix, a loop in the intermembrane space containing the highly conserved GMN motif connects to the $\alpha 9$ /TM2, which ends at the matrix side. A channel pore connecting intermembrane space and matrix is formed between the intertwined $\alpha 8$ /TM1 helices from five subunits. Four Mg^{2+} ions (termed Mg^{2+} -1, 2, 3, 4) were identified along the pore and two (termed Mg^{2+} -5, 6) were found in between neighboring soluble domains in the MRS2- Mg^{2+} structures (Fig. 1b, c and Supplementary Fig. 4).

Mg^{2+} -translocation pathway and gating mechanism

The five TM1 helices form the wall of the translocation pore, while mostly hydrophilic and charged side chains point to the center (Fig. 2a, b). Extra densities corresponding to four Mg^{2+} ions were found in the center along the pore (Fig. 2a, b and Supplementary Fig. 4). Although these extra densities are located at the center of the C5 symmetry axis and should therefore be interpreted carefully, they are also present in the non-symmetric C1 map and with that are unlikely to be artifacts generated by symmetry refinement (Supplementary Fig. 4b). The upper most Mg^{2+} (Mg^{2+} -1), closest to the mitochondrial intermembrane space is coordinated by the highly conserved GMN motif. Mg^{2+} -1 interacts with a ring of backbone carbonyl oxygens of G360 and amine group of N362 with a distance of 3.8 Å and 4.3 Å, respectively, indicating that the Mg^{2+} -1 is in hydrated form^{35,36}. Mg^{2+} -2, Mg^{2+} -3 and Mg^{2+} -4 are coordinated by a ring of hydroxyl oxygens of T346, carbonyl oxygens of N339, and carboxylic oxygens of D329 with a distance of 5.2 Å, 4.3 Å and 3.5 Å, respectively. A highly negatively charged surface was observed in the loop located

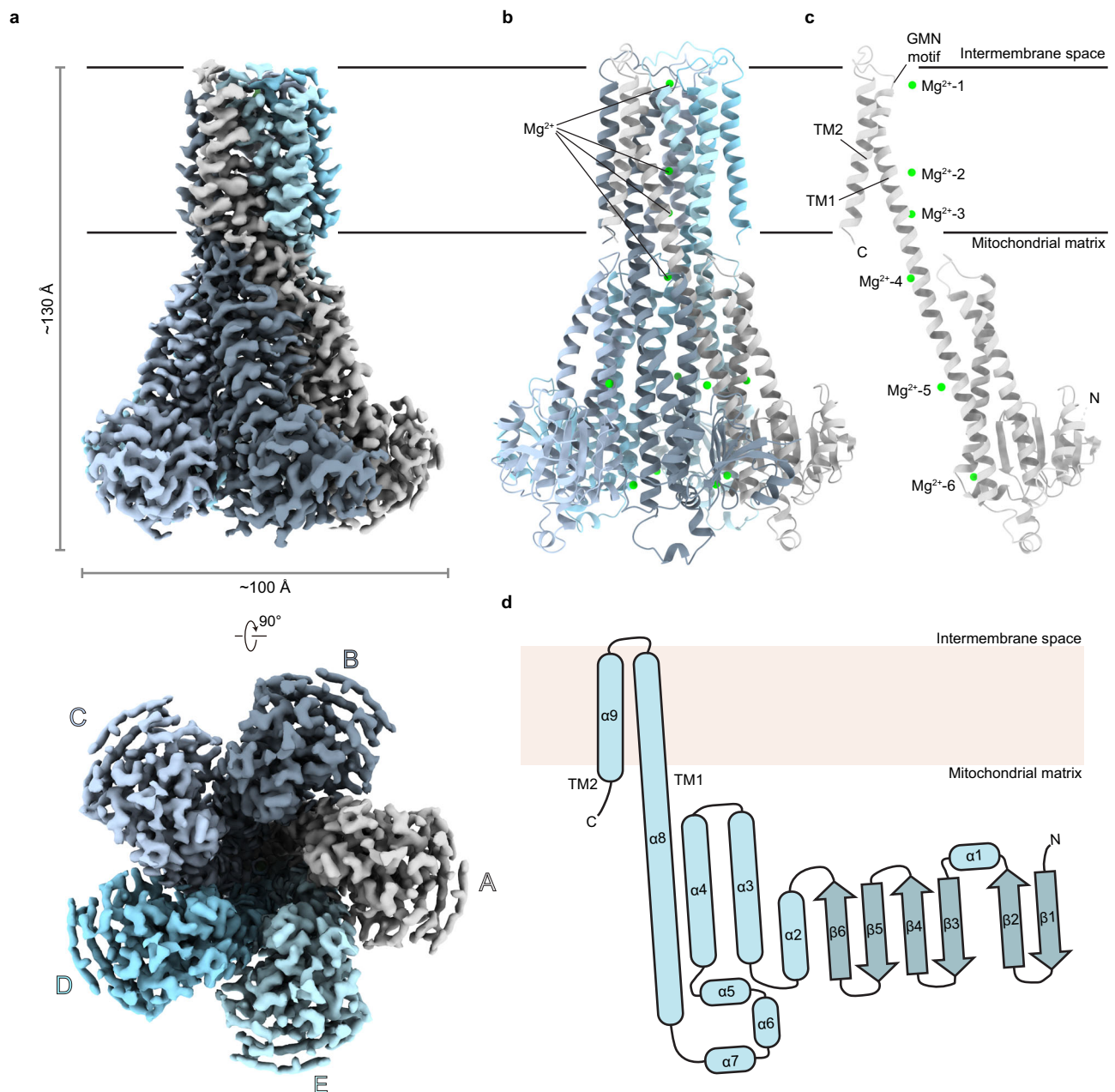


Fig. 1 | Structure of human MRS2 in the presence of Mg^{2+} . **a** The 2.8 Å cryo-EM density of MRS2 shown in side and bottom views. Density corresponding to each subunit is delineated by different colors. **b, c** Fitted structural model of

MRS2 shown as pentameric complex (**b**) and as single subunit (**c**). Magnesium ions bound to MRS2 are represented as green spheres. **d** Topology of MRS2 showing α -helices as rods and β -strands as slightly darker arrows.

at the intermembrane space and the soluble domain in the matrix facing the pore (Fig. 2a). A similar surface has also been observed in CorA and is believed to provide a pulling force for the transport of Mg^{2+} ions^{28,30}. The radius plot estimated by the program HOLE³⁷ shows the narrowest region of the pore is formed by a ring of M336 side chains, with a pore radius of 1.7 Å, followed by R332, and N362/G360, which is part of GMN motif (Fig. 2c). Owing to (1) the hydrophobicity of M336, (2) the repulsive positive charge at R332, and (3) a pore size that is clearly too narrow to allow hydrated Mg^{2+} to pass through, M336 and R332 likely represent candidates to act as gating residues capable of interrupting the ion flow. M336 is conserved among members of the CorA family, for instance, it corresponds to M291 in *TmCorA* (Supplementary Figs. 5, 6). *TmCorA* relies on hydrophobic gates M291, L294, M302 (referred to as MM stretch) to control Mg^{2+} flux^{38–40}. Interestingly, R332 is conserved among eukaryotes and for

example also found in yeast *Mrs2* but not in prokaryotic CorA homologs (Supplementary Fig. 6), suggesting the Mg^{2+} -translocation mechanism may be different in eukaryotic MRS2 compared to prokaryotic CorA. In MRS2, the positive charge of R332 is partially masked by D329 from the neighboring subunit one helix turn below, lowering the energy required for Mg^{2+} to pass through the R332 gate (Fig. 2b, d, e). Furthermore, we found a network of hydrogen bonds from S224 in the loop between soluble α -helix 3–4 of an adjacent subunit to N333 and the potential gating residue R332 (Fig. 2d, e). This network might allosterically link the soluble domain and pore gating residue R332, opening the possibility of a regulation mechanism in which the soluble domain also plays a role.

To evaluate the potential gating role of R332 and M336, we tested Mg^{2+} -translocation activity of R332A and M336A mutants by using a Mg^{2+} -dependent growth assay as described previously^{41,42}. The Mg^{2+} -

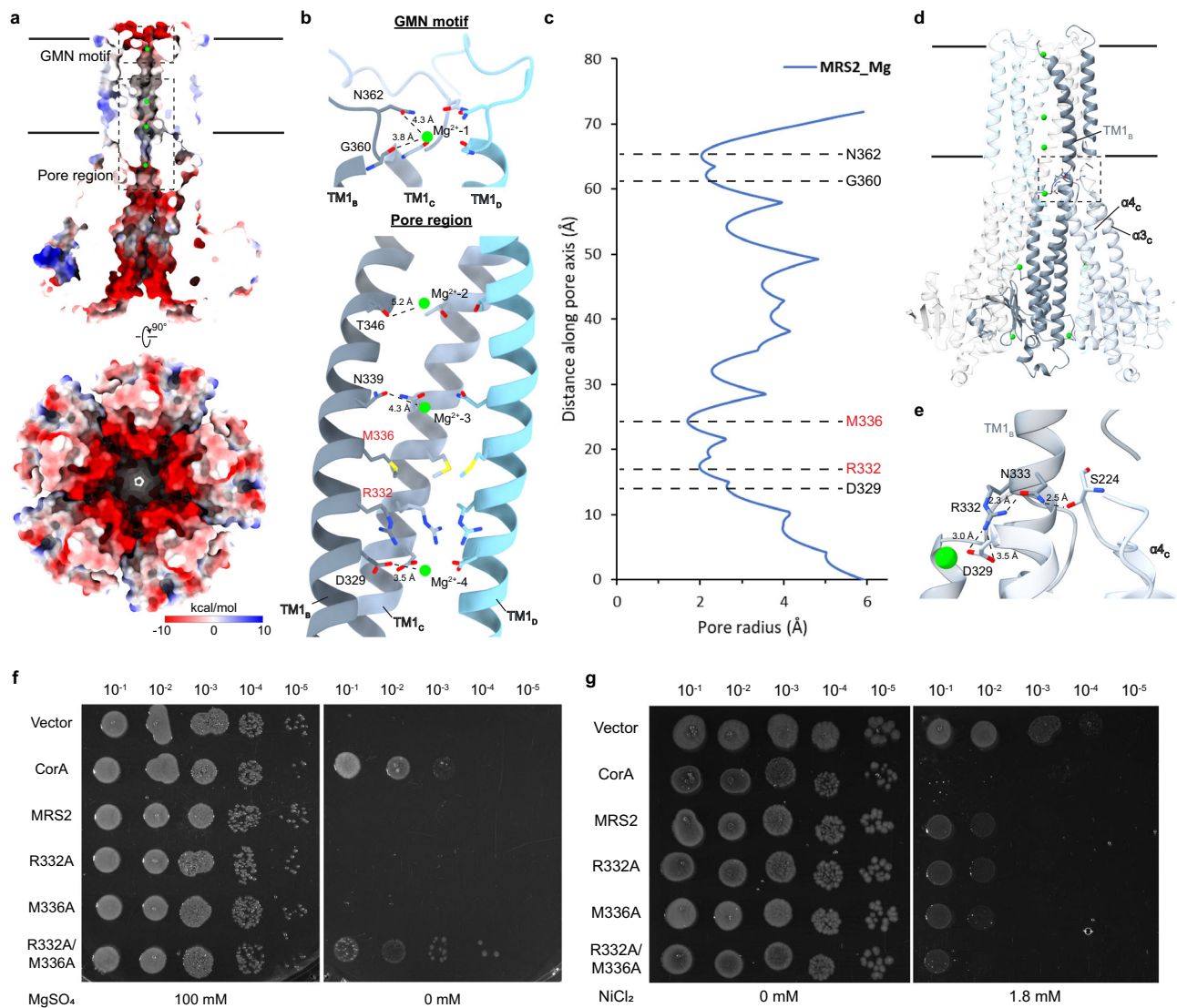


Fig. 2 | Mg²⁺-translocation pathway in MRS2. **a** Sliced side view of MRS2 illustrating the translocation pathway of Mg²⁺. The electrostatic potential of the surface is colored (from negative in red to positive in blue). Insets refer to regions highlighted in **(b)**. **b** Enlarged view of the GMN motif and pore region highlighting residues coordinating Mg²⁺ ions. Potential gating residues M336 and R332 are labeled in red. Only helices from subunits B, C, and D are shown for clearer illustration. **c** Pore radius plot of MRS2. **d, e** Network of hydrogen bonds connecting gating residue R332 and the loop between soluble α -helix 3–4 of an adjacent

subunit. Enlarged view of the interaction is shown in **(e)**. **f** Mg²⁺-auxotrophic growth complementation assay using the empty vector and *TmCorA* (controls), MRS2 and its mutants. Serially diluted Mg²⁺-auxotrophic *E. coli* (BW25113 Δ *mgtA*, Δ *corA*, Δ *yhiD* DE3) containing corresponding plasmids were spotted onto LB plates with and without MgSO₄, and grown at 30 °C. **g** Ni²⁺-sensitivity assay of BL21-(DE3) expressing *TmCorA* (control), MRS2 and its mutants. Serially diluted *E. coli* containing corresponding plasmids were spotted onto LB plates with and without 1.8 mM NiCl₂, and grown at 30 °C overnight.

auxotrophic *E. coli* strain BW25113 lacking the major Mg²⁺-transporters/channels (*mgtA*, *corA*, *yhiD*) can only grow either by supplementing the growth medium with high Mg²⁺ concentrations, or by complementation with a functional Mg²⁺-transporter/channel. Although expression of the WT *HsMRS2* and single gating mutants R332A or M336A is not sufficient to support the growth of the strain without the supplementation of Mg²⁺, double mutant R332A/M336A complements the growth synergistically (Fig. 2f).

A Ni²⁺-sensitivity assay has been employed in characterizing magnesium channel MgtE and its mutants previously^{41,43}. As coordination of Ni²⁺ is similar to that of Mg²⁺, and Mrs2 in yeast is able to translocate Ni²⁺ ions like CorA, although it has a higher selectivity for Mg²⁺ over Ni²⁺^{14,36}, we utilized the toxicity of Ni²⁺ to *E. coli* to evaluate Ni²⁺-uptake and *HsMRS2* channel activity. *E. coli* expressing WT *HsMRS2* shows a higher Ni²⁺-sensitivity over the negative control of *E. coli* with empty vector only, indicating *HsMRS2* does have some

channel activity in *E. coli* (Fig. 2g). Notably, there is no significant increase in Ni²⁺-sensitivity in single gating mutants R332A or M336A. Double gating mutant R332A/M336A shows increased Ni²⁺-sensitivity indicating more uptake of Ni²⁺ compared to WT or single mutants. Together with the complementation growth assay using the Mg²⁺-auxotrophic *E. coli* strain, it suggests both R332 and M336 residues are involved in gating of Mg²⁺ and other divalent cations in *HsMRS2*, while both gates need to be opened to allow Mg²⁺ to pass through.

Mg²⁺-binding sites in the soluble domain and their role in channel activity regulation

Two additional Mg²⁺ ions (Mg²⁺-5 and Mg²⁺-6) have been identified in the interface of neighboring subunits between their soluble N-terminal domains termed soluble sites 1 and 2 (Figs. 1b, c and 3a–c). The Mg²⁺ ions in soluble sites 1 and 2 are coordinated largely by negatively charged residues. Mg²⁺-5 and Mg²⁺-6 are hydrated, with some water

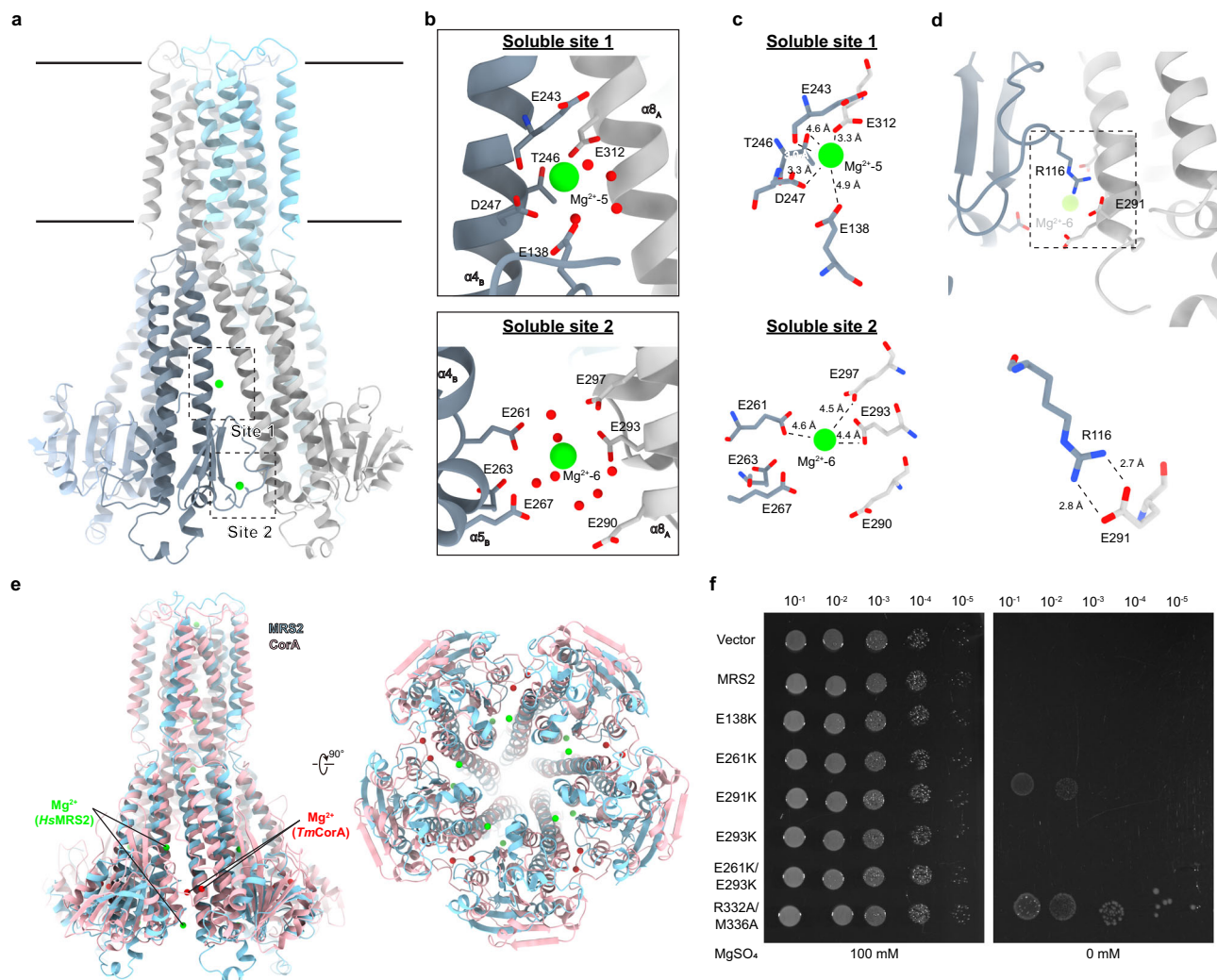


Fig. 3 | Two Mg^{2+} -binding sites in the MRS2 soluble domain and their role in channel activity regulation. **a** Two Mg^{2+} -binding sites are observed in the MRS2 soluble domain between subunits. Insets refer to regions highlighted in (b, c). **b** Mg^{2+} in the soluble domain coordinated by negatively charged residues including E243, D247, and E138 from one subunit and E312 from the neighboring subunit in soluble binding site 1. In the soluble binding site 2, Mg^{2+} is coordinated by E261, E263, and E267 from one subunit and E290, E293, E297 from the neighboring subunit. Water molecules in soluble sites 1 and 2 are shown in red spheres. **c** Detailed coordination of Mg^{2+} ions in the soluble site 1 and 2. **d** Salt bridge formed

between R116-E291 pair across subunits. Enlarged view of the R116-E291 is shown (lower panel). **e** Comparison of the Mg^{2+} -binding sites in the soluble domain between *HsMRS2* and *TmCorA*. Structure of *TmCorA* in closed state (PDB: 3JCF) in pink is overlaid with the MRS2 structure in blue. The Mg^{2+} ions in the soluble domain of *TmCorA* and MRS2 are represented as spheres in red and green, respectively. **f** Mg^{2+} -auxotrophic growth complementation assay using MRS2 and its mutants. Serially diluted Mg^{2+} -auxotrophic *E. coli* (BW25113 $\Delta mgtA$, $\Delta corA$, $\Delta yhiD$ DE3) containing corresponding plasmids were spotted onto LB plates with and without $MgSO_4$, and grown at 30 °C.

molecules around involved in coordination of Mg^{2+} with distances of 2.1 - 3.1 Å (Fig. 3b). Mg^{2+} -5 in site 1 interacts with side chains of T246, D247, E138, carboxyl oxygen of E243, and E312 from the neighboring subunit (Fig. 3b, c). Mg^{2+} -6 in site 2 is sandwiched between two negatively charged glutamate clusters from two adjacent subunits. E261, E297 and E293 contribute most in the coordination of Mg^{2+} -6 with distances of 4.4–4.6 Å, while E263, E267, and E290 are about 6–7 Å from the Mg^{2+} . The Mg^{2+} -binding sites in the soluble domain of MRS2 are located at different locations compared to *TmCorA* and *EcCorA* structures (Fig. 3e and Supplementary Fig. 5). Sequence alignment also shows the residues involved in soluble site 1 and 2 of MRS2 are not conserved in prokaryotic homologs (Supplementary Fig. 6). When overlaying the *HsMRS2* structure to the archaeal *MjCorA* X-ray structure³², in which 28 Mg^{2+} ions were modeled into the soluble domain in an asymmetric manner, the Mg^{2+} (atom spec: Mg^{E406}) between subunit E and A of *MjCorA* is close to soluble site 1 in MRS2; however, it is coordinated by E155, Y186, T90 and Q62, which is different to the groups of negatively charged residues (E138, E243, D247,

E312) in MRS2 (Supplementary Fig. 5). Interestingly, adjacent to soluble site 2 of *HsMRS2*, a salt bridge is observed between R116 from one subunit and E291 from the neighboring subunit, with a distance of 2.7–2.8 Å (Fig. 3d, Supplementary Fig. 4c).

It has been proposed that the Mg^{2+} -binding sites in the soluble domain of *TmCorA* serve as a Mg^{2+} -sensing motif, where unbinding of Mg^{2+} in those regions under low intracellular Mg^{2+} concentration facilitates channel opening and thereafter Mg^{2+} influx^{20,21}. Cryo-EM study of *TmCorA* shows that it undergoes dramatic asymmetric conformational changes of the soluble domain under low- Mg^{2+} conditions²⁷. To investigate whether soluble sites 1 and 2, along with the R116-E291 pair in *HsMRS2* are involved in channel regulation, glutamate residues involved in corresponding interactions were mutated to lysine residues and tested using the Mg^{2+} -dependent growth assay. Surprisingly, no noticeable change in growth was observed in the soluble Mg^{2+} -binding site mutants when compared to WT, while the E291K mutation disrupting the salt bridge between adjacent subunits promotes Mg^{2+} -dependent growth, suggesting higher MRS2 channel

activity (Fig. 3f). We speculate that the increase in MRS2 channel activity of the E291K mutant is a result of higher flexibility of the soluble domain that allows the propagation of movement to the TM regions leading to pore opening.

MRS2 structure under EDTA condition

To investigate whether MRS2 undergoes conformational changes in response to environmental Mg^{2+} concentrations, we depleted most of the free Mg^{2+} in purified MRS2 using dialysis and addition of EDTA and performed structural analysis by cryo-EM. The resulting structures of MRS2 in the presence of 1 mM EDTA (referred to as MRS2-EDTA) with C5 symmetry and without symmetry applied (C1) were determined at an average resolution of 3.3 Å and 3.6 Å, respectively, with the highest local resolution estimated to be 2.7 Å (Fig. 4a, b). Unlike *TmCorA*, no significant structural changes can be observed when EDTA was included in the sample buffer. The C α RMSD between MRS2- Mg^{2+} and MRS2-EDTA is 0.481 Å (Supplementary Fig. 7a). While inspecting the Mg^{2+} -binding sites found in the *HsMRS2* structure in the presence of Mg^{2+} , we do observe scattered densities in soluble site 2 but not soluble site 1 (Supplementary Fig. 7b). However, due to (1) the lower overall and local resolution of the MRS2-EDTA structure and (2) under EDTA conditions Mg^{2+} is not expected to be found in the position that is exposed to solvent, we speculate that these extra densities may represent water molecules coordinated by surrounding negatively charged residues. We have not modeled anything into these extra densities due to the high uncertainty. In the central pore regions, densities for Mg^{2+} -1, 2, 3 but not for Mg^{2+} -4 were observed along the pore of MRS2 even after dialysis and addition of EDTA which should remove most of the free Mg^{2+} in the solution (Fig. 4c). The GMN motif is known to have a high affinity towards Mg^{2+} with an estimated K_D of 1.3 μM ³⁶, which may be able to trap Mg^{2+} in the pore in the presence of EDTA. The conservation of Mg^{2+} -1, 2, 3 and the loss of Mg^{2+} -4, which is just below the R332/M336-rings, further suggests the gating properties of these residues and that MRS2 remains at low channel open probability without activation.

Discussion

In this study, we determined the structures of the human mitochondrial magnesium channel MRS2 in the presence of Mg^{2+} and under EDTA condition. MRS2 assembles into a homo-pentamer and displays an overall architecture similar to structures in the CorA family, with slight differences in the secondary structure arrangement (Supplementary Fig. 5). MRS2 possesses a central pore for ion

permeation. Near the intermembrane side of the pore, a conserved GMN motif is located to capture Mg^{2+} ions. Besides the naturally present high membrane potential across the inner mitochondrial membrane, a negative surface potential at the pore-facing side of the soluble domain provides a pulling force for Mg^{2+} influx. Along the pore, R332 and M336 have been identified as the main gating residues. Double mutations of these residues significantly increase Mg^{2+} - and Ni^{2+} -uptake, suggesting a higher channel activity. Single mutants did not change the channel activity compared to the wild-type. Loss of the Mg^{2+} ion below the M336/R332 gate towards to mitochondrial matrix in the MRS2-EDTA structure further supports the role of M336 and R332 in gating. Strikingly, the R332 gate does not seem to be conserved among prokaryotic CorA homologs, suggesting that MRS2 may adopt a different Mg^{2+} -translocation and regulatory mechanism.

In *TmCorA*, two Mg^{2+} -binding sites (M1 and M2) have been identified in the soluble domains of adjacent subunits^{28–30}. Mg^{2+} ions are coordinated by D89 and D253 at the M1 site, and D253, E88, L12, D175 at the M2 site. It has been proposed that these M1 and M2 sites serve as divalent cation sensors responding to intracellular ion concentrations and modulating channel activation. Unbinding of Mg^{2+} in the low affinity M1 and M2 sites under low intracellular Mg^{2+} concentration facilitates channel opening. *TmCorA* D253K mutation abolished the Mg^{2+} -dependent protease susceptibility²⁸ and Mg^{2+} -dependent channel inhibition²⁰. Previous EPR, cryo-EM and MD-simulation studies of CorA show dramatic movements of the soluble domain under EDTA condition and suggest that the inter-subunit binding of Mg^{2+} in the soluble domain holds the five subunits in the closed, less flexible conformation^{20,27,44}. In the present human MRS2- Mg^{2+} structure, two inter-subunit Mg^{2+} ions were also identified but these are in different positions when compared to those in CorA (Fig. 3e and Supplementary Fig. 5), and employ different sets of residues in Mg^{2+} coordination (Supplementary Figs. 5 and 6). Mutating residues in soluble sites 1 and 2 from glutamate (E) to lysine (K) shows no observable differences when compared to WT in the Mg^{2+} -dependent growth assay. One possibility is that in MRS2 the E to K mutation facilitates salt bridge formation to the glutamate residues of the adjacent subunit, promoting the closed conformation of the channel. This idea is supported by the loss of function phenotype of the D253K *TmCorA* mutant using cellular and fluorescence based Mg^{2+} -uptake assays³⁸. On the other hand, introducing a E291K mutation in *HsMRS2*, which disrupts a salt bridge between adjacent subunits and likely mimics low- Mg^{2+} conditions, shows a gain of function phenotype (Fig. 3f), potentially due to

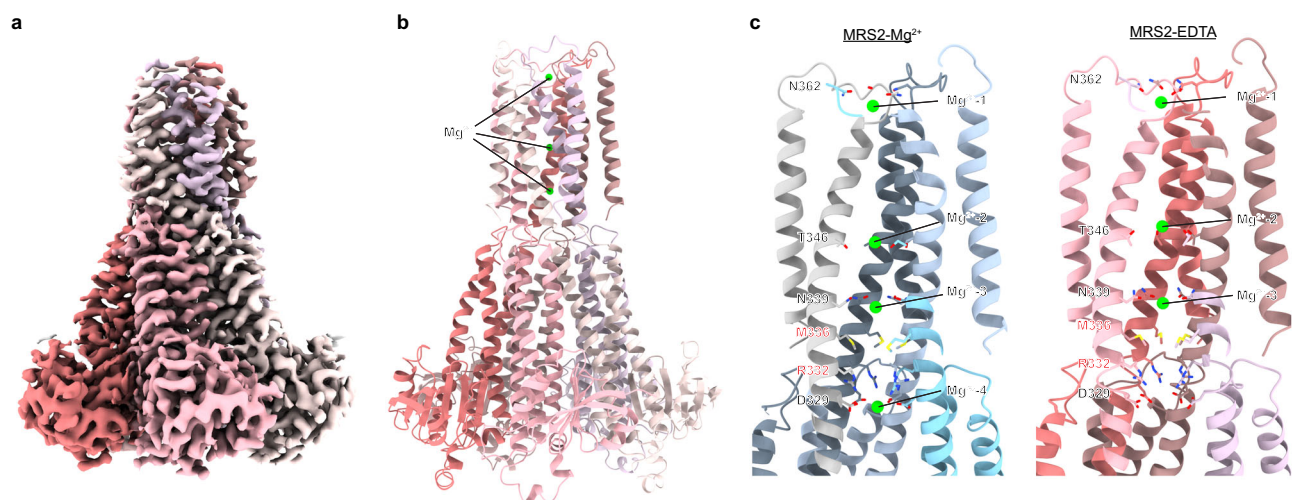


Fig. 4 | Structure of MRS2 under EDTA condition. **a** Cryo-EM density map of MRS2 in the presence of 1 mM EDTA at 3.3 Å. **b** Model of the MRS2-EDTA structure. **c** Comparison of MRS2- Mg^{2+} and MRS2-EDTA showing the loss of Mg^{2+} beneath the R332-ring.

increased flexibility in the soluble domain which might be associated with the regulation of MRS2 channel activity.

During our final manuscript preparation, additional structures of human MRS2 (hMrs2) under various conditions have been reported⁴⁵. As in the present study, hMrs2 assembles into a homo-pentamer and displays a similar structure in the presence of Mg²⁺, low EDTA, high EDTA and without Mg²⁺ and EDTA (termed hMrs2-rest). In general, the reported structures⁴⁵ are in agreement with ours, with 0.652 Å C α RMSD between structures in the presence of Mg²⁺. Two Mg²⁺ ions are identified along the pore of the reported structures, corresponding to Mg²⁺-1, 4 in our study. Two additional Mg²⁺ ions (Mg²⁺-2, 3) have been found in both of our structures, coordinated by a ring of hydroxyl oxygens of T346 and carbonyl oxygens of N339 with a distance of 5.2 Å and 4.3 Å, respectively. We reason that the additional two Mg²⁺ ions identified is likely due to higher Mg²⁺ concentration (40 mM) in our sample, compared to 20 mM used in the previous publication⁴⁵. Interestingly, a tentative Cl⁻ has been placed in the R332-ring which is proposed to facilitate Mg²⁺-permeation by masking the electrostatic repulsion caused by the R332-ring⁴⁵. Besides, MD-simulation demonstrates that the presence of Cl⁻ around the R332-ring lowers the energy barrier for Mg²⁺ permeation. When we built the MRS2-Mg²⁺ and MRS2-EDTA models based on our cryo-EM maps, we also see a consistent density above the R332-ring in both structures (Supplementary Fig. 8). Based on the coordination by the R332 residues, we speculate the density may be contributed by a water molecule or possibly an anion such as a chloride ion. Although it is tempting to speculate a chloride ion around the positively charged R332-ring, the presence of a chloride ion in the pore is challenged by the negatively charged pore entry near the GMN motif and the D329-ring, which create a barrier for a chloride ion to enter the pore from either side (Fig. 2a, b). Of note, a previous MD-simulation study on CorA has observed that hydration events occur along the pore including the hydrophobic MM stretch, lowering the free energy barrier for Mg²⁺ permeation⁴⁰. Indeed, water molecules near polar residues T343, N362, E368, and carbonyl oxygens of G356 and V357 along the pore can be found in our MRS2-Mg²⁺ structure. Together, we support an assignment of a water molecule in the density instead of a chloride ion. However, due to the resolution limit in both studies, the identity of the density near R332 remains to be confirmed by additional experimental approaches, such as X-ray anomalous scattering.

Besides a pore dilation and increase in gate flexibility⁴⁰, other proposed mechanisms of CorA channel opening include helix rotation of TMs displacing the hydrophobic gating residues⁴⁶, as well as relaxation/bending motion of the soluble domains coupled with TM movement leading to gate opening^{38,39} (Supplementary Fig. 9). Here, we observed a connection between gating residue R332 and the soluble domain of an adjacent subunit via hydrogen bonds (Fig. 2d, e). We speculate that movement of the soluble domain has a role in the opening of the pore gates in MRS2 (Supplementary Fig. 9e), which is further supported by the increased channel activity upon disrupting the inter-subunit salt bridge between R116 and E291 as mentioned above.

In addition to the gating residue R332, which shows no significant increase in mitochondrial Mg²⁺-uptake when mutated to R332A, R332K, or R332E in the recent study⁴⁵, we identified M336 as another gating residue. We found that a single mutation of R332 showed no significant change in channel activity unless M336 was mutated as well, suggesting both gates need to be opened simultaneously or sequentially in order to allow for Mg²⁺ permeation. A previous electrophysiological study shows that matrix Mg²⁺ reduces the open probability of yeast Mrs2, suggesting a negative feedback mechanism¹⁴. In our study, we observed the loss of Mg²⁺-4 around the D329-ring in the MRS2-EDTA structure (Fig. 4c). It is tempting to propose that the D329-ring plays a role in the negative feedback mechanism of MRS2. Under low matrix Mg²⁺ concentration, Mg²⁺-unbinding from D329 may allow the interaction between D329 and

R332, masking the positive charge of R332 and lowering the energy barrier of Mg²⁺ to pass through the R332 gate (Supplementary Fig. 9d). When the Mg²⁺ concentration is high in the mitochondrial matrix, Mg²⁺ is captured by the D329-ring, decoupling the interaction between D329 and R332, re-establishing a barrier by the positive R332-ring. However, the detailed mechanism of how the gating residues are regulated remains to be investigated. Elucidation of the MRS2 structure in an open state will help to address this question.

In summary, our study identifies N-terminal residue 71 as the first amino acid of human MRS2 after protein translocation into the inner mitochondrial membrane and cleavage of its MTP, and reports structures of human MRS2 in the presence and absence of Mg²⁺ at 2.8 Å and 3.3 Å, respectively. We identified R332 and M336 as gating residues and a for stability and channel activity important salt bridge between R116 and E291, which provides further insight into the Mg²⁺ permeation and regulatory mechanism in MRS2.

Methods

Protein expression and purification

Full-length human MRS2 (Uniprot Q9HD23) conjugated with a FLAG tag at the C-terminus was expressed in Expi293F cells (Thermo Fisher Scientific, A14527). Cells at a density of 2.0–3.0 × 10⁶ cells/ml were transfected with the MRS2-encoding pCMV plasmid using polyethylenimine (PEI) following the protocol described previously⁴⁷. Cells were harvested 48 h after transfection, and resuspended in Lysis buffer (20 mM HEPES, 150 mM NaCl, 10% [v:v] glycerol, 40 mM MgCl₂, pH 7.3) supplemented with cOmplete, EDTA-free protease inhibitor cocktail (Roche). After cell disruption by sonication on ice, the membrane fraction was collected by ultracentrifugation at 100,000 × *g* for 1 h at 4 °C. The pelleted membranes were resuspended with Lysis buffer and pelleted again at 100,000 × *g* for 1 h. The membrane pellets were flash frozen in liquid nitrogen and stored at –80 °C until use. For solubilization, membranes at a protein concentration of ~4 mg/ml were solubilized with 1% (w:v) n-dodecyl- β -*D*-maltopyranoside (DDM) (Anatrace) and 0.1% cholesteryl hemisuccinate Tris salt (CHS) (Anatrace) for 2 h at 4 °C, followed by another round of ultracentrifugation to remove insoluble material. The supernatant was incubated with ANTI-FLAG M2 Affinity Gel (Millipore) on an end-over-end rotator for 2 h at 4 °C. The MRS2-bound beads were incubated in Lysis buffer containing 1% lauryl maltose-neopentyl glycol (LMNG) for 30 min at 4 °C, followed by extensive washing with Washing buffer (Lysis buffer supplemented with 0.01% LMNG). Proteins were eluted with 0.2 mg/ml 3 \times FLAG peptide. Eluted fractions were concentrated to ~3 mg/ml using a 50 kDa cut-off centrifugal filter and loaded onto a Superdex 200 Increase 3.2/300 size-exclusion column (Cytiva) with SEC buffer (20 mM HEPES, 150 mM NaCl, 40 mM MgCl₂, 0.003% LMNG, pH 7.3). Peak fractions (~0.5 mg/ml) were collected for cryo-EM grid preparation. For the MRS2 sample in 1 mM EDTA, the sample was prepared in the same procedure except that the sample was dialyzed overnight to remove MgCl₂, followed by size-exclusion chromatography with 1 mM EDTA SEC buffer (20 mM HEPES, 150 mM NaCl, 1 mM EDTA, 0.003% LMNG, pH 7.3). The protein fractions were resolved and analyzed using 4–12% Bis-Tris gel (Invitrogen) for SDS-PAGE and 4–16% Bis-Tris gel (Invitrogen) for BN-PAGE.

N-terminal sequencing

Purified MRS2 was resolved by SDS-PAGE, followed by transferring to methanol activated PVDF membrane in a XCell Mini-Cell Blot Module (Thermo Fisher) at 30 V for 2 h. The MRS2 band on PVDF was stained with Ponceau S, excised and shipped to Creative Proteomics for N-terminal sequencing via Edman degradation.

Negative staining electron microscopy

3 μ L of MRS2 (0.02 mg/mL) was applied on a glow discharged carbon-coated 400 square mesh copper grid (EMS) and incubate for 1 min.

The grid was then blotted by filter paper (Whatman) and washed once with 3 μL of Nano-W negative staining solution (Nanoprobes) followed by incubation with 3 μL of Nano-W for 1 min. The grid was blotted to remove excess staining solution and air-dried by waving. Images were recorded using an FEI Tecnai T20 TEM operated at 200 kV with a direct electron detector K2 Summit (Gatan Inc.). Data was collected using SerialEM⁴⁸ at a nominal magnification of 25,000 \times , a pixel size of 3.04 $\text{\AA}/\text{px}$, and defocus range between $-1.5\ \mu\text{m}$ and $-2.5\ \mu\text{m}$. A total of 459 images was collected. Image processing was performed using cisTEM v1.0.0⁴⁹. 215,448 particles were picked from the micrographs after CTF estimation, extracted with a box of 108 px ($\sim 328\ \text{\AA}$) and analyzed by 2D classification.

Cryo-EM grid preparation and data collection

3 μL purified MRS2 at approximately 0.5 mg/ml was applied to a glow-discharged 400-mesh R 1.2/1.3 Cu grid (Quantifoil). The cryo grids were blotted for 6 s at 4 $^{\circ}\text{C}$ and 95%, and plunge-frozen into liquid ethane using a Leica EM GP2 (Leica) and stored in liquid nitrogen. The grids were screened on an FEI Tecnai T20 TEM before data collection.

Cryo-EM datasets were acquired with SerialEM⁴⁸ using a Titan Krios (FEI, now ThermoFisher Scientific) operated at 300 kV and equipped with an energy filter and K3 camera (Gatan Inc.). Movies of 50 frames with a dose of 1 $e^{-}/\text{\AA}^2$ per frame (50 $e^{-}/\text{\AA}^2$ total dose) were recorded at a nominal magnification of 105,000 \times , corresponding to a physical pixel size of 0.83 $\text{\AA}/\text{px}$ (super-resolution pixel size 0.415 $\text{\AA}/\text{px}$) in CDS mode at a dose rate of 10 $e^{-}/\text{px}/\text{s}$ and a defocus range of -0.7 to $-2.0\ \mu\text{m}$. In total, 3991 and 9656 movies were collected for MRS2-Mg²⁺ and MRS2-EDTA, respectively (Supplementary Table 1).

Cryo-EM data processing

The overall workflow of image processing is illustrated in Supplementary Fig. 2. All processing was performed within cryoSPARC v3.3.2⁵⁰. Movies were processed with patch motion correction and patch CTF estimation. Good 2D class averages generated from ~ 1000 manually picked particles served as templates for automatic particle picking.

For MRS2-Mg²⁺, 1,568,444 particles were picked and extracted at 1 \times binned pixel size of 0.83 \AA with a box size of 320 px ($\sim 266\ \text{\AA}$). Particles were then subjected to 2D classification to remove junk particles. 573,010 good particles selected from one round of 2D classification was subjected to ab-initio reconstruction ($K=2$) and heterogenous refinement ($K=2$) with C1 symmetry to further sort particles. Non-uniform refinement was performed with 450,554 selected particles, followed by local motion correction and CTF refinement to correct for beam-tilt, spherical aberrations, and per-particle defocus parameters. Non-uniform refinement with polished particles resulted in maps at 2.8 \AA (with C5 symmetry applied) and 3.1 \AA (with C1 symmetry applied), according to gold-standard FSC = 0.143 criterion (Supplementary Fig. 2).

For MRS2-EDTA, 4,802,706 particles were picked and extracted at 4 \times binned pixel size of 3.32 \AA and sorted by one round of 2D classification, ending up with 1,755,556 particles. Ab-initio reconstruction ($K=3$) was performed with the subset of particles after 2D classification, followed by heterogenous refinement ($K=3$) using all particles with C1 symmetry was applied to remove junk particles. Particles from one class (2,237,316 particles) were re-extracted at 1 \times binned pixel size of 0.83 \AA and subjected to non-uniform refinement followed by another round of heterogenous refinement ($K=2$) to further sort particles. Final non-uniform refinement by using 1,744,117 particles yielded maps at 3.3 \AA (with C5 symmetry applied) and 3.6 \AA (with C1 symmetry applied) according to gold-standard FSC = 0.143 criterion.

The summary of data collection and imaging processing parameters are shown in Supplementary Tables 1 and 2. The cryo-EM maps

of MRS2-Mg²⁺ (C1 and C5) and MRS2-EDTA (C1 and C5) have been made available and have the following accession codes: EMD-41624, EMD-41629, EMD-41628 and EMD-41630, respectively.

Model building and refinement

For the atomic model of MRS2-Mg²⁺, predicted MRS2 AlphaFold⁵¹ structure (AF-Q9HD23-F1) was used as an initial model. The initial model was rigid-body fitted into the local resolution filtered map using UCSF Chimera v.1.16⁵². The model was then manually rebuilt in COOT v.0.9.7⁵³ using the local resolution filtered map, which was generated from refinement with C5 applied. The Mg²⁺ ions assigned in the pore regions were confirmed in the C1 map. Loop regions (residues 174–181, 273–287) were built with the unsharpened map. Iterative rounds of manual refinement in COOT and real-space refinement in Phenix v.1.20.1-4487⁵⁴ were performed. For the MRS2-EDTA structures, models were generated from multiple rounds of manual refinement and real-space refinements with the final model of MRS2-Mg²⁺ as initial model. The quality of the model and fit to the density was assessed using MolProbity⁵⁵ and Phenix⁵⁴. All structural figures were prepared using UCSF Chimera v.1.16⁵² or UCSF ChimeraX v.1.4⁵⁶. PDBs have been made available together with the EM maps with the following PDB IDs: 8TUL (MRS2-Mg²⁺) and 8TUP (MRS2-EDTA).

Subcellular localization of MRS2

Expi293F cells at a density of 2.0–3.0 $\times 10^6$ cells/ml were transfected with the MRS2-GFP or MRS2(71-443)-GFP encoding pCMV plasmid using polyethylenimine (PEI) following the protocol described previously⁴⁷. 24 h after transfection, the cells were stained with 100 nM MitoTracker Red (Thermo Fisher Scientific) or 1 μM ER-Tracker Red (Thermo Fisher Scientific) for 30 min at 37 $^{\circ}\text{C}$. The cells were washed twice with PBS and imaged using a Zeiss LSM 880 confocal laser scanning microscope.

Mg²⁺-dependent *E. coli* growth assay

The Mg²⁺-auxotrophic *E. coli* strain (BW25113 ΔmgtA , ΔcorA , ΔyhiD DE3), which has been used previously^{41,42}, was transformed with His-*TmCorA*, MRS2(71-443)-FLAG, its mutants or without insert in a pET28a backbone. The transformants were inoculated and grown in kanamycin (50 $\mu\text{g}/\text{mL}$) containing LB medium (LBK) supplemented with 100 mM MgSO₄, shaking at 250 rpm and 37 $^{\circ}\text{C}$ overnight. The overnight cultures were used to inoculate fresh LBK in a 1:100 ratio and grown until they reached an OD₆₀₀ of 0.6. The bacterial cultures were then diluted 10-fold serially with LBK medium, spotted onto LBK agar plates containing 0.1 mM IPTG and 0 or 100 mM MgSO₄, and incubated at 30 $^{\circ}\text{C}$ for 2 days. Plates were imaged using ChemiDoc MP Imaging System (Bio-rad).

Ni²⁺-sensitivity assay

BL21(DE3) (Sigma, CMC0014) was transformed with His-*TmCorA*, MRS2(71-443)-FLAG, its mutants or without insert in a pET28a backbone. The transformants were inoculated and grown in LBK medium, shaking at 250 rpm and 37 $^{\circ}\text{C}$ overnight. The overnight cultures were used to inoculate fresh LBK in a 1:100 ratio and grown until they reached an OD₆₀₀ of 0.6. The bacterial cultures were then diluted 10-fold serially with LBK medium, spotted onto LBK agar plates containing 0.1 mM IPTG, and 0 or 1.8 mM NiCl₂, and incubated at 30 $^{\circ}\text{C}$ overnight. Plates were imaged using ChemiDoc MP Imaging System (Bio-rad).

Reporting summary

Further information on research design is available in the Nature Portfolio Reporting Summary linked to this article.

Data availability

The data that support this study are available from the corresponding authors upon request. Cryo-EM maps have been deposited in the

Electron Microscopy Data Bank (EMDB) under accession codes [EMD-41624](#) (Cryo-EM structure of the human MRS2 magnesium channel under Mg²⁺ condition); [EMD-41628](#) (Cryo-EM structure of the human MRS2 magnesium channel under Mg²⁺-free condition); [EMD-41629](#) (Cryo-EM structure of the human MRS2 magnesium channel under Mg²⁺ condition (C1 map)); and [EMD-41630](#) (Cryo-EM structure of the human MRS2 magnesium channel under Mg²⁺-free condition (C1 map)). The atomic coordinates have been deposited in the Protein Data Bank (PDB) under accession codes [8TUL](#) (Cryo-EM structure of the human MRS2 magnesium channel under Mg²⁺ condition); and [8TUP](#) (Cryo-EM structure of the human MRS2 magnesium channel under Mg²⁺-free condition). The source data for Supplementary Fig. 1b, c are provided in the Source Data file. Source data are provided with this paper.

References

- Jahnen-Dechent, W. & Ketteler, M. Magnesium basics. *Clin. Kidney J.* **5**, i3–i14 (2012).
- de Baaij, J. H., Hoenderop, J. G. & Bindels, R. J. Magnesium in man: implications for health and disease. *Physiol. Rev.* **95**, 1–46 (2015).
- Mathew, A. A. & Panonnummal, R. ‘Magnesium’-the master cation-as a drug-possibilities and evidences. *Biometals* **34**, 955–986 (2021).
- DiNicolantonio, J. J., Liu, J. & O’Keefe, J. H. Magnesium for the prevention and treatment of cardiovascular disease. *Open Heart* **5**, e000775 (2018).
- Saris, N. E., Mervaala, E., Karppanen, H., Khawaja, J. A. & Lewenstam, A. Magnesium. An update on physiological, clinical and analytical aspects. *Clin. Chim. Acta* **294**, 1–26 (2000).
- Yamanaka, R., Shindo, Y. & Oka, K. Magnesium is a key player in neuronal maturation and neuropathology. *Int. J. Mol. Sci.* **20**, <https://doi.org/10.3390/ijms20143439> (2019).
- Romani, A. M. Cellular magnesium homeostasis. *Arch. Biochem. Biophys.* **512**, 1–23 (2011).
- Rodriguez-Zavala, J. S. & Moreno-Sanchez, R. Modulation of oxidative phosphorylation by Mg²⁺ in rat heart mitochondria. *J. Biol. Chem.* **273**, 7850–7855 (1998).
- Pilchova, I., Klacanova, K., Tatarikova, Z., Kaplan, P. & Racay, P. The involvement of Mg(2+) in regulation of cellular and mitochondrial functions. *Oxid. Med. Cell Longev.* **2017**, 6797460 (2017).
- Marchi, S. & Pinton, P. The mitochondrial calcium uniporter complex: molecular components, structure and pathophysiological implications. *J. Physiol.* **592**, 829–839 (2014).
- Bui, D. M., Gregan, J., Jarosch, E., Ragnini, A. & Schweyen, R. J. The bacterial magnesium transporter CorA can functionally substitute for its putative homologue Mrs2p in the yeast inner mitochondrial membrane. *J. Biol. Chem.* **274**, 20438–20443 (1999).
- Zsurka, G., Gregan, J. & Schweyen, R. J. The human mitochondrial Mrs2 protein functionally substitutes for its yeast homologue, a candidate magnesium transporter. *Genomics* **72**, 158–168 (2001).
- Kolisek, M. et al. Mrs2p is an essential component of the major electrophoretic Mg²⁺ influx system in mitochondria. *EMBO J.* **22**, 1235–1244 (2003).
- Schindl, R., Weghuber, J., Romanin, C. & Schweyen, R. J. Mrs2p forms a high conductance Mg²⁺ selective channel in mitochondria. *Biophys. J.* **93**, 3872–3883 (2007).
- Piskacek, M., Zotova, L., Zsurka, G. & Schweyen, R. J. Conditional knockdown of hMRS2 results in loss of mitochondrial Mg(2+) uptake and cell death. *J. Cell Mol. Med.* **13**, 693–700 (2009).
- Yamanaka, R. et al. Mitochondrial Mg(2+) homeostasis decides cellular energy metabolism and vulnerability to stress. *Sci. Rep.* **6**, 30027 (2016).
- Kuramoto, T. et al. A mutation in the gene encoding mitochondrial Mg(2+) channel MRS2 results in demyelination in the rat. *PLoS Genet* **7**, e1001262 (2011).
- Daw, C. C. et al. Lactate elicits ER-Mitochondrial Mg(2+) dynamics to integrate cellular metabolism. *Cell* **183**, 474–489 e417 (2020).
- Madaris, T. R. et al. Limiting Mrs2-dependent mitochondrial Mg(2+) uptake induces metabolic programming in prolonged dietary stress. *Cell Rep.* **42**, 112155 (2023).
- Dalmas, O., Sompornpisut, P., Bezanilla, F. & Perozo, E. Molecular mechanism of Mg²⁺-dependent gating in CorA. *Nat. Commun.* **5**, 3590 (2014).
- Pfoh, R. et al. Structural asymmetry in the magnesium channel CorA points to sequential allosteric regulation. *Proc. Natl Acad. Sci. USA* **109**, 18809–18814 (2012).
- Khan, M. B. et al. Structural and functional characterization of the N-terminal domain of the yeast Mg²⁺ channel Mrs2. *Acta Crystallogr. D Biol. Crystallogr.* **69**, 1653–1664 (2013).
- Uthayabalan, S., Vishnu, N., Madesh, M. & Stathopoulos, P. B. The human MRS2 magnesium-binding domain is a regulatory feedback switch for channel activity. *Life Sci. Alliance* **6**, <https://doi.org/10.26508/lsa.202201742> (2023).
- Almagro Armenteros, J. J. et al. Detecting sequence signals in targeting peptides using deep learning. *Life Sci. Alliance* **2**, <https://doi.org/10.26508/lsa.201900429> (2019).
- Teufel, F. et al. SignalP 6.0 predicts all five types of signal peptides using protein language models. *Nat. Biotechnol.* **40**, 1023–1025 (2022).
- Fukasawa, Y. et al. MitoFates: improved prediction of mitochondrial targeting sequences and their cleavage sites. *Mol. Cell Proteom.* **14**, 1113–1126 (2015).
- Matthies, D. et al. Cryo-EM structures of the magnesium channel CorA reveal symmetry break upon gating. *Cell* **164**, 747–756 (2016).
- Payandeh, J. & Pai, E. F. A structural basis for Mg²⁺ homeostasis and the CorA translocation cycle. *EMBO J.* **25**, 3762–3773 (2006).
- Lunin, V. V. et al. Crystal structure of the CorA Mg²⁺ transporter. *Nature* **440**, 833–837 (2006).
- Eshaghi, S. et al. Crystal structure of a divalent metal ion transporter CorA at 2.9 angstrom resolution. *Science* **313**, 354–357 (2006).
- Lerche, M., Sandhu, H., Flockner, L., Högbohm, M. & Rapp, M. Structure and cooperativity of the cytosolic domain of the CorA Mg(2+) channel from Escherichia coli. *Structure* **25**, 1175–1186 e1174 (2017).
- Guskov, A. et al. Structural insights into the mechanisms of Mg²⁺ uptake, transport, and gating by CorA. *Proc. Natl Acad. Sci. USA* **109**, 18459–18464 (2012).
- Gati, C., Stetsenko, A., Slotboom, D. J., Scheres, S. H. W. & Guskov, A. The structural basis of proton driven zinc transport by ZntB. *Nat. Commun.* **8**, 1313 (2017).
- Stetsenko, A., Stehantsev, P., Dranenko, N. O., Gelfand, M. S. & Guskov, A. Structural and biochemical characterization of a novel ZntB (CmaX) transporter protein from Pseudomonas aeruginosa. *Int. J. Biol. Macromol.* **184**, 760–767 (2021).
- Dudev, T. & Lim, C. Importance of metal hydration on the selectivity of Mg²⁺ versus Ca²⁺ in magnesium ion channels. *J. Am. Chem. Soc.* **135**, 17200–17208 (2013).
- Dalmas, O. et al. A repulsion mechanism explains magnesium permeation and selectivity in CorA. *Proc. Natl Acad. Sci. USA* **111**, 3002–3007 (2014).
- Smart, O. S., Neduveilil, J. G., Wang, X., Wallace, B. A. & Sansom, M. S. HOLE: a program for the analysis of the pore dimensions of ion channel structural models. *J. Mol. Graph* **14**, 354–360 (1996). 376.
- Payandeh, J. et al. Probing structure-function relationships and gating mechanisms in the CorA Mg²⁺ transport system. *J. Biol. Chem.* **283**, 11721–11733 (2008).
- Chakrabarti, N., Neale, C., Payandeh, J., Pai, E. F. & Pomes, R. An iris-like mechanism of pore dilation in the CorA magnesium transport system. *Biophys. J.* **98**, 784–792 (2010).

40. Neale, C., Chakrabarti, N., Pomorski, P., Pai, E. F. & Pomes, R. Hydrophobic gating of ion permeation in magnesium channel CorA. *PLoS Comput. Biol.* **11**, e1004303 (2015).
41. Jin, F. et al. The structure of MgtE in the absence of magnesium provides new insights into channel gating. *PLoS Biol.* **19**, e3001231 (2021).
42. Hattori, M. et al. Mg(2+)-dependent gating of bacterial MgtE channel underlies Mg(2+) homeostasis. *EMBO J.* **28**, 3602–3612 (2009).
43. Tomita, A. et al. ATP-dependent modulation of MgtE in Mg(2+) homeostasis. *Nat. Commun.* **8**, 148 (2017).
44. Nemchinova, M., Melcr, J., Wassenaar, T. A., Marrink, S. J. & Guskov, A. Asymmetric CorA gating mechanism as observed by molecular dynamics simulations. *J. Chem. Inf. Model* **61**, 2407–2417 (2021).
45. Li, M. et al. Molecular basis of Mg(2+) permeation through the human mitochondrial Mrs2 channel. *Nat. Commun.* **14**, 4713 (2023).
46. Nordin, N. et al. Exploring the structure and function of Thermotoga maritima CorA reveals the mechanism of gating and ion selectivity in Co2+/Mg2+ transport. *Biochem. J.* **451**, 365–374 (2013).
47. Longo, P. A., Kavran, J. M., Kim, M. S. & Leahy, D. J. Transient mammalian cell transfection with polyethylenimine (PEI). *Methods Enzymol.* **529**, 227–240 (2013).
48. Mastronarde, D. N. Automated electron microscope tomography using robust prediction of specimen movements. *J. Struct. Biol.* **152**, 36–51 (2005).
49. Grant, T., Rohou, A. & Grigorieff, N. cisTEM, user-friendly software for single-particle image processing. *eLife* **7**, <https://doi.org/10.7554/eLife.35383> (2018).
50. Punjani, A., Rubinstein, J. L., Fleet, D. J. & Brubaker, M. A. cryoSPARC: algorithms for rapid unsupervised cryo-EM structure determination. *Nat. Methods* **14**, 290–296 (2017).
51. Jumper, J. et al. Highly accurate protein structure prediction with AlphaFold. *Nature* **596**, 583–589 (2021).
52. Pettersen, E. F. et al. UCSF Chimera—a visualization system for exploratory research and analysis. *J. Comput. Chem.* **25**, 1605–1612 (2004).
53. Emsley, P., Lohkamp, B., Scott, W. G. & Cowtan, K. Features and development of Coot. *Acta Crystallogr. D Biol. Crystallogr.* **66**, 486–501 (2010).
54. Afonine, P. V. et al. Real-space refinement in PHENIX for cryo-EM and crystallography. *Acta Crystallogr. D Struct. Biol.* **74**, 531–544 (2018).
55. Williams, C. J. et al. MolProbity: More and better reference data for improved all-atom structure validation. *Protein Sci.* **27**, 293–315 (2018).
56. Goddard, T. D. et al. UCSF ChimeraX: Meeting modern challenges in visualization and analysis. *Protein Sci.* **27**, 14–25 (2018).

Acknowledgements

We thank Joshua Zimmerberg, Jennifer Petersen, and Paul Blank for access to a Tecnai T20 electron microscope and Zeiss LSM 880 confocal microscope; Allison Zeher and Rick K. Huang for support on the Krios; and Stéphane Mahé and Joe Cometa for technical support on the T20 and Krios. We are grateful to Prof. Dr. Koichi Ito for providing us the Mg²⁺-auxotrophic *E. coli* strain (BW25113 Δ mgtA, Δ corA, Δ yhiD DE3). We also like to thank Eduardo Perozo and Lesley Earl for helpful comments on the manuscript. This research was supported by the Division of

Intramural Research of the Eunice Kennedy Shriver National Institute of Child Health and Human Development, NIH (grant NICHD intramural project ZIA HD008998). This work utilized the computational resources of the NIH HPC Biowulf cluster (<http://hpc.nih.gov>).

Author contributions

L.T.F.L. performed protein expression, purification, negative-staining EM, cryo-EM screening, cryo-EM data collection, image processing, and the Mg²⁺-dependent growth assay. J.B. performed the Ni²⁺-sensitivity assay and the Mg²⁺-dependent growth assay. F.Z. helped with cryo-EM data collection. L.T.F.L. and D.M. designed the study, performed model building, structural analysis, made figures and wrote the manuscript. All authors discussed the results and contributed to the manuscript preparation.

Funding

Open Access funding provided by the National Institutes of Health (NIH).

Competing interests

The authors declare no competing interests.

Additional information

Supplementary information The online version contains supplementary material available at <https://doi.org/10.1038/s41467-023-42599-3>.

Correspondence and requests for materials should be addressed to Doreen Matthes.

Peer review information *Nature Communications* thanks Sergei Sukharev and the other, anonymous, reviewer(s) for their contribution to the peer review of this work. A peer review file is available.

Reprints and permissions information is available at <http://www.nature.com/reprints>

Publisher's note Springer Nature remains neutral with regard to jurisdictional claims in published maps and institutional affiliations.

Open Access This article is licensed under a Creative Commons Attribution 4.0 International License, which permits use, sharing, adaptation, distribution and reproduction in any medium or format, as long as you give appropriate credit to the original author(s) and the source, provide a link to the Creative Commons licence, and indicate if changes were made. The images or other third party material in this article are included in the article's Creative Commons licence, unless indicated otherwise in a credit line to the material. If material is not included in the article's Creative Commons licence and your intended use is not permitted by statutory regulation or exceeds the permitted use, you will need to obtain permission directly from the copyright holder. To view a copy of this licence, visit <http://creativecommons.org/licenses/by/4.0/>.

This is a U.S. Government work and not under copyright protection in the US; foreign copyright protection may apply 2023